

Submitted to The Astrophysical Journal

Three-Dimensional Simulations of Spherical Accretion Flows with Small-Scale Magnetic Fields

Igor V. Igumenshchev

*Laboratory for Laser Energetics, University of Rochester
250 East River Road, Rochester, NY 14623*

iigu@lle.rochester.edu

ABSTRACT

Spherical (nonrotating) accretion flows with small-scale magnetic fields have been investigated using three-dimensional, time-dependent MHD simulations. These simulations have been designed to model high-resolution (quasi) steady accretion flows in a wedge computational domain that represents a small fraction of the full spherical domain. Subsonic and supersonic (super-fast-magnetosonic) accretion flows have been considered. Two accretion regimes have been studied: conservative, or radiatively inefficient, and nonconservative, in which the heat released in magnetic reconnections is completely lost. The flows in both regimes are turbulent. They show the flattened radial density profiles and reduction of the accretion velocities and mass accretion rates in comparison with hydrodynamic Bondi flows. In the conservative regime, the turbulence is more intensive and supported mostly by thermal convection. In the nonconservative regime, the turbulence is less intensive and supported by magnetic buoyancy and various magnetic interactions. We have concluded that steady, supersonic spherical accretion cannot be developed in the presence of small-scale magnetic fields.

Subject headings: accretion, accretion disks — black hole physics — convection — MHD — turbulence

1. Introduction

Mass accretion onto a central gravitational body plays an important role in the formation and evolution of a large variety of astrophysical objects such as planets, stars, galactic nuclei,

galaxies, and clusters of galaxies (see Frank, King & Raine 1992). Depending on the amount of the angular momentum ℓ_0 , which the accreting mass carries at the outer boundary radius R_{out} , accretion flows can take either a disk-like or spherical-like form. Flows with relatively high angular momentum, $\ell_0 \simeq \sqrt{GM R_{\text{out}}}$, where G is the gravitational constant and M is the central mass, form centrifugally supported accretion disks (e.g., Shakura 1972). Flows with low angular momentum, $\ell_0 \ll \sqrt{GM R_{\text{out}}}$, can form spherical or quasi-spherical accretion flows at radii $R \gtrsim \ell_0^2/GM$ in which the centrifugal force is weak and not sufficient to balance gravity (Illarionov & Sunyaev 1975). The theoretical study of spherical accretion flows is based on an analytical solution discovered several decades ago by Bondi (1952). This solution describes the idealized case of isentropic nonmagnetic accretion flows. Since that time, the theory of spherical accretion has been significantly developed so that it now includes an understanding the role of different physical mechanisms (such as radiative cooling and heating, magnetic field dissipation, thermal and radiation transports, etc.) and more realistic inner and outer boundary conditions (for reviews, see Frank *et al.* 1992; Kato, Fukue, & Mineshige 1998). More recent studies of spherical accretion considered convection (Marković 1995), accretion onto a magnetic dipole (Toropin *et al.* 1999), magnetic diffusivity due to turbulence (Shadmehri 2004), and vorticity (Krumholz, McKee, & Klein 2005).

This paper continues the numerical study of radiatively inefficient spherical (nonrotating) accretion flows with magnetic fields conducted by Igumenshchev & Narayan (2002, hereafter IN; also see Pen, Matzner, & Wong 2003 for a similar study). IN have demonstrated, with help of three-dimensional MHD simulations, that the effects of a magnetic field can significantly modify the structure of Bondi-type flows. They argued that even initially weak magnetic fields can produce dramatic changes. The main reason for these changes is the local, nonuniform release of the thermal energy during the dissipation of tangled magnetic fields in reconnections. This release suppresses the inward motion of mass and results in the development of turbulence that is mainly supported by thermal convection. The dissipation of a magnetic field in reconnections is compensated by the efficient amplification of the radial field component in spherical convergent flows (Shvartsman 1971). IN have developed a simple analytical theory of spherical convection-dominated accretion flows (spherical CDAFs¹), which is similar, with regards to the involved basic physics, to the theory of rotating CDAFs (Narayan, Igumenshchev, & Abramowicz 2000; Quataert & Gruzinov 2000). This theory predicts the flattened radial density profile $\rho \propto R^{-1/2}$ in contrast to the steeper density profile in asymptotic Bondi flows, $\rho \propto R^{-3/2}$ (see the appendix, eq. [A6]). Because of this flattened profile, the mass accretion rate in spherical CDAFs is expected to be significantly lower than the Bondi mass accretion rate in flows with the equivalent outer boundary

¹Note that IN used instead the name “convection-dominated Bondi flows” which we do not adopt here.

conditions;

$$\dot{M} \sim \dot{M}_{\text{Bondi}} \left(\frac{R_{\text{in}}}{R_{\text{out}}} \right), \quad (1)$$

where R_{in} is the inner radius of the flows. These properties make the spherical CDAF solution to be a prominent candidate for explaining the phenomenon of dim galactic nuclei contained supermassive black holes, including our Galactic center Sgr A* (e.g., Melia 1992; Baganoff *et al.* 2001, 2003; Quataert 2002; Ghez *et al.* 2003; Ho, Terashima, & Okajima 2003; Soria *et al.* 2006), in which accretion disks are typically not observed. Also, spherical CDAFs can be employed to explain the problem of missing isolated neutron stars in our Galaxy (Treves & Colpi 1991; Blaes & Madau 1993; Turolla *et al.* 1994; Belloni, Zampieri, & Campana 1997; Toropina *et al.* 2003; Perna *et al.* 2003) and the observed properties of isolated stellar mass black holes (e.g., Fujita *et al.* 1998; Agol & Kamionkowski 2002).

The generality of the numerical results of IN and Pen *et al.* (2003) were limited in the important aspect that no steady or quasi-steady accretion flows were obtained. These authors studied transient states of the flows, which originated because of specific initial conditions and involved moving outward shocks. These results also suffered from insufficient numerical resolution, especially in the innermost region of the flows. In addition, the assumption of an initial bipolar magnetic field in IN resulted in the domination of a large-scale poloidal field and doughnut-like density distribution near the black hole at the later evolution time (note that similar field topology was proposed by Bisnovatyi-Kogan & Ruzmaikin 1974). Unless such large-scale poloidal field can be naturally present in some objects, other possible field configurations, such as a small-scale field with zero net magnetic flux, can likely be natural too in spherical accretion flows. The main goal of the present study is the investigation of the role of small-scale magnetic fields in such flows.

In the numerical aspect, we overcome some of the limitations of the IN’s approach employing a new simulation design. In this design, we assume a permanent injection of mass and magnetic field into the computational domain that allows us to obtain steady or quasi-steady accretion flows after performing long-time evolution simulations. The numerical resolution has been improved by adopting spherical coordinates and conducting simulations in the wedge computational domain, which represents a small fraction of the full spherical domain (see Fig. 1). The injected field is assumed to have a small-scale component in the form of radially extended magnetic loops with a zero net magnetic radial flux (see Fig. 2). Modifications of the simulation technique allow us to investigate two limiting energetic regimes: conservative (or radiatively inefficient) and non-conservative (in which the heat from magnetic reconnections is completely lost).

The paper is organized as follows. In Section 2 we describe the simulation technique, initial and boundary conditions, and algorithm of the mass and magnetic field injection.

Section 3 presents numerical results, and in Section 4 we discuss these results and make final conclusions. We reproduce some analytic solutions of hydrodynamic accretion flows, including Bondi solution, in the appendix.

2. Simulation Technique

We use the numerical method, which is similar to that used by IN and Igumenshchev, Narayan, & Abramowicz (2003). The method solves the system of ideal MHD equations (e.g., Landau & Lifshitz 1987), which describe the dynamics of nonself-gravitating plasmas in the central gravitational field. Originally, the method employed a nonconservative numerical scheme that solves the internal energy equation, which includes the reconnection heat term Q (for more details see IN);

$$\rho \frac{d\epsilon}{dt} = -P_g \nabla \cdot \mathbf{v} + Q, \quad (2)$$

where ρ is the density, ϵ is the specific internal energy, P_g is the gas pressure, and \mathbf{v} is the velocity. Test simulations have shown that MHD solutions obtained using equation (2) conserve the total energy quite poorly because of artificial losing or gaining energy in numerical reconnections. In some our test cases, the relative error of the total energy conservation was up to 10%. To solve this problem, the method has been modified by adding a conservative option. Using this option, the method solves the total energy equation

$$\frac{\partial}{\partial t} \left(\rho \frac{v^2}{2} + \rho \epsilon + \frac{B^2}{8\pi} \right) = -\nabla \cdot \mathbf{q} \quad (3)$$

instead of equation (2). Here \mathbf{B} is the magnetic induction and \mathbf{q} is the total energy flux per unit square. Note that in finite-difference MHD schemes the magnetic field is reconnected on scales in which the minimum is limited by the gridsize. Typically, this gridsize is much larger than the physical reconnection scales in the studied problems. Therefore, the finite-difference schemes, including our scheme, can not accurately represent all the details in the process of reconnection. For our purposes, however, the provided level of accuracy is sufficient. This situation is somewhat analogous to the representation of shocks in finite-difference hydrodynamic schemes in which the numerical shock thickness is also limited by the gridsize.

In all our simulations, we have used the ideal gas equation of state

$$P_g = (\gamma - 1)\rho\epsilon \quad (4)$$

and assumed the adiabatic index $\gamma = 5/3$.

This method employs the three-dimensional spherical coordinates (R, θ, ϕ) . The computational domain is limited by a narrow four-facet wedge located at the equatorial plane as shown in Figure 1. The domain is extended from R_{in} to R_{out} in the radial direction and over θ_0 and ϕ_0 degrees in the polar and azimuthal directions. We have assumed $\theta_0 = \phi_0 = \pi/16$ and the number of angular gridpoints $N_\theta \times N_\phi = 30 \times 30$. These points are uniformly spaced in both θ and ϕ directions. Gridpoints in the radial direction are spaced logarithmically so that the three-dimensional numerical cells at any radius take an approximately cubic shape. This provides the direction-independent local spatial resolution in the simulations. The number of the radial gridpoints $N_R = 303$, which corresponds to $R_{\text{out}}/R_{\text{in}} = 10$.

2.1. Boundary Conditions

We have used three different sets of boundary conditions assumed at the azimuthal, polar, and radial boundaries, respectively, of the wedge computational domain (see Fig. 1). The periodic boundary conditions for both fluid and magnetic field are applied at the azimuthal boundaries. At the polar boundaries, we use the conditions that no streamlines and magnetic lines can go inside/outside through these boundaries. This is achieved by applying the reflection boundary conditions for fluid and assuming the continuous tangential and reflection normal magnetic components across the polar boundaries.

At the inner R_{in} and outer R_{out} radial boundaries, we apply the absorbing boundary conditions for a fluid. This means that the mass can flow freely out of the computational domain, but no mass is allowed to return from outside. Conditions for the magnetic field are assumed considering “ghost” boundary zones located on the outside of the computational domain. We assume that these zones can contain only a radial magnetic field, whose strength is determined from the divergence-free constraint $\nabla \cdot \mathbf{B} = 0$. Numerical tests have shown that a mass with a frozen-in tangled magnetic field can freely flow out through these radial boundaries without the effects of field or mass accumulation.

Our absorbing boundary conditions at R_{in} qualitatively correctly mimic the conditions near the black hole horizon where matter is free falling in the strong gravity field and the radial component of the magnetic field dominates the tangential component (e.g., Thorne, Price, & MacDonald 1986). In the case of accreting stars with rigid surfaces such as white dwarfs and neutron stars, which can also have magnetospheres, the inner boundary condition will depend on the radiative efficiency of the flows. Radiatively inefficient plasma will probably form a slowly accreting ($\dot{M} \ll \dot{M}_{\text{Bondi}}$) subsonic accretion flows, similar to that “a tenuous continuation of the star” discussed by Bondi (1952). If plasma efficiently radiates its thermal energy near the stars’ surfaces (e.g., Shapiro & Salpeter 1975), the considered

absorbed inner boundary conditions can be adequate for accretion flows far away from these surfaces.

2.2. Injection of Mass

To obtain steady, or quasi-steady, accretion flows, we permanently inject mass into the computational domain. The main problem here is to minimize the consequences of the interaction of outflows, which can originate during simulations, and the injected mass. We have employed an injection algorithm, which has some resemblance to the injection algorithm used by Igumenshchev & Abramowicz (1999) in simulations of rotating accretion flows.

We assume that the mass is steadily injected inside a thin spherical layer with the radius R_{inj} , which is located closely to the outer absorbing boundary at R_{out} . This mass is distributed uniformly over θ and ϕ directions and has zero velocity. Under the action of gravity, the larger fraction of the injected mass forms an accretion flow. The smaller fraction of this mass could escape through R_{out} because of a thermal spread and interactions with outflows.

The injected mass is characterized by the specific internal energy ϵ_0 , which determines two regimes of hydrodynamic accretion – subsonic and supersonic. The critical value $(\epsilon_0)_{\text{crit}} \approx \epsilon_{\text{vir}}$ where

$$\epsilon_{\text{vir}} \equiv GM/R_{\text{inj}} \quad (5)$$

separates these regimes: $\epsilon > (\epsilon_0)_{\text{crit}}$ corresponds to subsonic flows and $\epsilon < (\epsilon_0)_{\text{crit}}$ corresponds to supersonic flows (see the appendix).

2.3. Injection of a Magnetic Field

The injected mass can also carry a magnetic field that is associated with it. The field is injected assuming that only the poloidal component A_θ of the vector potential \mathbf{A} is nonzero in the injected mass; the other two components, A_R and A_ϕ , are set to zero. In this way we can produce B_R and B_ϕ components, which obey

$$B_R = -\frac{1}{R \sin \theta} \frac{\partial A_\theta}{\partial \phi}, \quad B_\phi = \frac{1}{R} \frac{\partial}{\partial R} (R A_\theta). \quad (6)$$

Three different magnetic field configurations have been used in simulations: purely (unipolar) radial, purely toroidal, and loop configurations. The former two configurations

have been chosen to test our numerical method. The purely radial field is generated at the beginning of simulations assuming that

$$A_\theta = B_{\text{inj}} R_{\text{inj}} \frac{R_{\text{inj}}}{R} \phi, \quad (7)$$

where B_{inj} is the magnetic induction at R_{inj} . This field remains unchanged during simulations by virtue of the conservation of the radial magnetic flux confined in the wedge computational domain.

Two other field configurations, purely toroidal and loop fields, are formed by permanently injecting the corresponding field at R_{inj} . This field injection is tightened to the mass injection and performed by correcting A_θ inside the injection layer at each time step as follows:

$$A'_\theta = A_\theta + \xi \Delta A, \quad (8)$$

where ΔA is an increment and ξ is a correction factor $0 \leq \xi \leq 1$. The increment ΔA depends on the assumed field configuration. In the case of purely toroidal field,

$$\Delta A = B_0 R_{\text{inj}}, \quad (9)$$

where $B_0 = \sqrt{8\pi\gamma(\gamma-1)\epsilon_0\Delta\rho/\beta_0}$ and $\Delta\rho$ is the density of the injected mass. In the case of loop field,

$$\Delta A = B_0 R_{\text{inj}} \frac{R_{\text{inj}}}{R} \frac{\sin(m\phi)}{m}, \quad (10)$$

where the parameter m determines the number of azimuthal sectors in which the radial magnetic field periodically changes direction. A combination of two such sectors forms a magnetic loop. In the present simulations, we have assumed two magnetic loops in the computational domain as illustrated in Figure 2.

The correction factor ξ in equation (8) is used to maintain the strength of the injected field at a given level determined in terms of the plasma $\beta \equiv P_g/P_m$, where $P_m = B^2/8\pi$ is the magnetic pressure. We assume that

$$\xi = \min \left[1, \max \left(0, \frac{\langle \beta \rangle - \beta_0}{\beta_0} \right) \right], \quad (11)$$

where β_0 is a parameter, which determines the field strength, and $\langle \beta \rangle$ is the β averaged over the volume of the injection layer.

3. Numerical Results

We initiate simulations from a static, nonmagnetic, very low-density medium that fills the entire computational domain. Accretion flows are created by steadily injecting the

mass into this medium at R_{inj} . These flows generally go through an initial transient phase before relaxing to a steady or quasi-steady state. The transient phase typically takes a few tens ($\simeq 10 - 30$) of the free-fall time, $t_{\text{ff}} \approx 0.67 R_{\text{out}}^{3/2} / \sqrt{GM}$, and includes the formation and dissipation of shocks and nonlinear waves. The hydrodynamic flows and MHD flows with the purely radial and toroidal fields have finally been relaxed to steady states. The MHD flows with the loop field have remained time variable, or quasi-steady, even after the completion of the transient phase.

IN discussed in detail the role of magnetic reconnections in spherical accretion flows with $\beta \sim 1$. This role depends on the amount of reconnection heat contributed to the gas internal energy. We have considered two extreme energetic regimes, conservative and non-conservative. In the conservative regime, the dissipated magnetic energy is fully transformed into the heat. Models in this regime have been calculated by employing the total energy equation (3). In the nonconservative regime, the dissipated magnetic energy is totally lost and does not produce any heat. In this regime, we employ the internal energy equation (2) in which the dissipation term Q has been set to zero. Note that the term described the artificial heat from shocks has been retained in equation (2).

The study of these conservative/nonconservative accretion regimes can be astrophysically motivated. The conservative regime can corresponds to the very high accretion rate flows with $\dot{M} \gg \dot{M}_{\text{Edd}}$, which do not radiate much energy due to the large optical depth of the flows (e.g., Katz 1977). Here $\dot{M}_{\text{Edd}} = 4\pi GM / \sigma_T m_p c$ is the Eddington accretion rate, σ_T is the Thomson-scattering cross-section, and m_p is the proton mass. Another option for the conservative regime is the very low accretion rate flows, $\dot{M} \ll \dot{M}_{\text{Edd}}$, if one assumes that the energy released in magnetic reconnections primary does to the ions, which cannot loose this energy efficiently via the usually considered electron-ion Coulomb collisions because of the tenuous plasma (e.g., Esin *et al.*). There is another possibility, however, that a significant fraction of the reconnection energy will go to electrons, which can efficiently radiate this energy by variety of mechanisms (Bisnovaty-Kogan & Lovelace 1997, 2000; Quataert & Gruzinov 1999). The latter possibility provides the additional cooling mechanism for ions, which in some circumstance could be more efficient than the Coulomb collisions, making the low, or even very low, accretion rate flows to be nonconservative, or radiatively efficient.

We shall describe models that are either subsonic or supersonic and differed by the strength of the injected fields, amount of the heat release in reconnections, and field configuration. The model parameters are listed in Table 1. For convenience, we have divided all these models into three groups: Bondi-type flows (Models A1-A4), subsonic MHD flows (Models B1 and B2), and supersonic MHD flows (Models C1 and C2). The structure of the Bondi-type flows, i.e. flows without magnetic fields or with the fields of special topology, is

similar to the structure of Bondi (1952) solution and well approximated by nonmagnetic analytic solutions discussed in the appendix. The structure of the latter two groups of models is significantly modified because of magnetic fields. We shall describe these groups separately.

3.1. Bondi-type flows

Bondi-type flows (Models A1-A4, see Table 1) have been calculated to verify our numerical method and obtain reference models. These flows are steady and laminar. Models A1-A3 represent subsonic flows and Model A4 represents a supersonic flow. Models A1 and A4 have no magnetic field, and thus describe hydrodynamic flows. Model A2 has the purely toroidal but sufficiently subequipartition ($\beta \gg 1$) magnetic field and Model A3 has the uniformly ordered strong ($\beta \lesssim 1$) radial magnetic field. In the latter two cases, the magnetic field does not affect the structure and dynamics of the flows and these cases are almost equivalent to Model A1.

We shall describe the evolution and structure of subsonic Bondi-type flows using Model A1 as a representative example. This model has evolved from the initial state (see §2) to a steady state through the transient phase. This phase includes the formation of temporal shocks and waves, which many times propagate inward and outward in the radial direction, reflecting from the inner and outer boundaries, before complete disappearance after $t \simeq 20 - 30 t_{\text{ff}}$. The final flow in Model A1 is steady, effectively one-dimensional, and described by the analytic solution (eqs. [A4] and [A8]). This solution suggests that Model A1 represents a part of the flow located deeply inside the Bondi radius, $R_{\text{out}} = 0.0371 R_B$, and, therefore, this model can be closely approximated by an asymptotic Bondi solution (A6), which appears in the limit $R \ll R_B$. Figure 3 shows selected properties of Model A1 (short-dashed lines) as functions of the radius. These properties include the distribution of density ρ (left top panel); gas pressure P_g (left middle panel); relative temperature $T/T_{\text{vir}} = \epsilon/(GM/R)$ (left bottom panel); Mach number $\mathcal{M} = v/c_s$ (right top panel), where $c_s = \sqrt{\gamma P/\rho}$ is the sound speed; relative radial velocity v/v_{ff} (right middle panel); and relative accretion rate (right bottom panel). In the latter case, the accretion rate is normalized to the mass injection rate (see §2). Because the flow is steady, the accretion rate is independent of the radius. Note that about 90% of the injected mass forms inflow. The other 10% escapes through R_{out} because of a thermal spread.

For comparison, Figure 3 also shows a self-similar solution (A9) in which $\mathcal{M} = 1$ (long-dashed lines). This solution is “boundary free” and has asymptotic Bondi profiles $\rho \propto R^{-3/2}$ and $P_g \propto R^{-5/2}$ throughout. Note that Model A1 demonstrates slightly flatter density and pressure profiles, which can be explained by the deviation of R/R_B from the zerolimit.

Model A2 has the weak and dynamically unimportant toroidal magnetic field $\beta \gg 1$. In all other aspects, Models A2 and A1 are similar. Using Model A2, we have tested the ability of our numerical method to accurately model the passive transport of magnetic field. The magnetic flux conservation requires that the toroidal field near the equatorial part of a spherical flow is changed as

$$B_\phi \propto (Rv)^{-1}. \quad (12)$$

This leads to $B_\phi \propto R^{-1/2}$ and $P_m \propto R^{-1}$ for the self-similar velocity profile $v \propto R^{-1/2}$. Because Model A2 has the steeper velocity profile, however, the actual profile of P_m obtained in this model is accordingly flatter and its slope is fully consistent with estimate (12).

Model A3 has a uniform radial magnetic field. This field is changed with the radius as $B_R \propto R^{-2}$ and therefore $P_m \propto R^{-4}$. The strength of the field has been chosen such that it has $\beta = 30$ at R_{out} and $\beta \simeq 0.1$ at R_{in} . The simulations have shown no effects from the flow transition from the subequipartition to superequipartition field regions. We shall see later, however, that such a transition causes significant changes in the flows with the loop field.

Note the artificial nature of the field topology assumed in Model A3 that represents a small sector of the spherically symmetric monopole field. Such a field can not have magnetic reconnections, which actually play an important role in realistic MHD flows. Accretion flows in a strong unipolar magnetic field similar to that considered in Model A3, however, can occur at magnetic poles of neutron stars and white dwarfs.

Properties of the supersonic hydrodynamic Model A4 are shown in Figure 4 with short-dashed lines. The density and pressure profiles in this model demonstrate nonmonotonic behavior at the outer region and approaching the asymptotic Bondi powerlaws $\rho \propto R^{-3/2}$ and $P_g \propto R^{-5/2}$ at the inner region (see left top and left middle panels in Fig. 4). The Mach number and accretion velocity (see right top and right middle panels in Fig. 4) show a significant increase inward from the outer boundary. All these properties of Model A4 are in good agreement with analytic solution (A11), which fits Model A4, assuming $R_{\text{out}}/\tilde{R}_B = 0.071$ (see the appendix).

3.2. Subsonic MHD Flows

Subsonic MHD flows are represented by Models B1 and B2 (see Table 1) and have a dynamically important magnetic field $\beta \sim 1-10$. This field is injected into the computational domain in the form of magnetic loops stretched in the radial direction (see Fig. 2). The strength of the field is determined by the parameter β_0 (see Table 1 and eq. [11]). The total energy is conserved in Model B1, whereas the energy released in magnetic reconnections is

completely lost in Model B2.

Simulations of Models B1 and B2 have been initiated from the steady hydrodynamic Model A1 by gradually increasing the strength of the injected magnetic field to provide a smooth transition from nonmagnetic to magnetic flows. Even in this case, however, Models B1 and B2 have been settled into their final quasi-steady states after passing through the initial transient phases. The final quasi-steady states are turbulent and characterized by random variations of all quantities on all spatial scales from the grid size to the size of the computational domain. The amplitude of these variations, however, is not large and the time-averaged properties of the accretion flows remain unchanged on the large time scale. The turbulence in Models B1 and B2 is clearly originated because of the effects of the magnetic field.

Figures 5–9 illustrate the structure of conservative Model B1, showing the snapshots of two-dimensional distributions of selected quantities in the equatorial cross section of the three-dimensional computational domain. Figure 5 represents the density distribution, which shows clearly recognizable small-scale (with respect to the scale R) density variations of the relative amplitude $\simeq 2$. The lower and higher density regions typically take the form of filaments, which are predominantly extended in the radial direction. These radially extended structures can also be seen in the velocity streamlines in Figure 6. The streamlines form a complicated flow pattern consisting of the radially extended narrow inflowing/outflowing streams and small-scale vortices.

The time-dependent flow pattern in Model B1 demonstrates the randomly repeating events of the interchange instability. In these events, colder, denser matter is accumulated above (i.e., far from the center) the region with hotter, lower density matter. With time, this denser matter begins to move down through the low-density region, forming a characteristic radially inflowing dense stream. Such a stream typically forms a “mushroom” at its head and propagates about half a radius inward from the radius of origin. At the same time, the stream carries a frozen-in magnetic loop whose field strength is amplified because of a radial convergence of the stream. The example snapshot of magnetic lines in Figure 7 shows many such magnetic loops resulting from the interchange instability. During the subsequent evolution, the inflowing radial streams are fragmented into small pieces. This fragmentation is typically triggered by reconnections of the oppositely directed magnetic lines confined in the streams. The reconnections locally release energy and produce a hot low-density matter. This matter has a positive buoyancy and forms narrow low-density outflows.

Figure 8 shows the snapshot of the plasma β . The spatial distribution of β and, accordingly, magnetic field is highly nonuniform. The small-scale, high- β regions, $\beta \gtrsim 100$, cover the entire computational domain and correspond to the weak field regions, which are

typically associated with reconnection regions. The large number of these regions clearly indicates the high efficiency of the reconnection dissipation. The low- β regions, $\beta \lesssim 1$, or, accordingly, the strong field regions are typically elongated in the radial direction and associated with the inflowing streams. The field in such regions becomes especially strong, $\beta \ll 1$, in the innermost part of the flow, $R \lesssim 2R_{\text{in}}$, where the high-velocity inflowing streams dominate in the flow pattern.

The chaotic inward and outward turbulent motions in Model B1 are only partially supported by magnetic interactions, whereas the more important support is provided by thermal convection. As discussed earlier, magnetic reconnections are very efficient in the considered model and produce hot, low-density, narrow outflows. Sometimes several such outflows can coalesce and form a large convective bubble, which moves outward easier and faster. The representative example of such a bubble can be seen in Figure 5 as the low-density region near the outer boundary and, in Figure 9, as the corresponding increase of the specific entropy. Later in time, this particular bubble has escaped through R_{out} . Figure 9 also shows many other local regions of high specific entropy. These regions typically coincide with the lower density regions in Figure 5, have positive velocities, and can therefore be identified as convective bubbles. However, not all such bubbles will be able to escape through R_{out} . A significant part of these bubbles will be pulled inward, mixed with the inflowing cold matter, and absorbed at R_{in} .

To make the argument concerning the development of convection more quantitative, we have calculated a one-dimensional time- and angle-averaged distribution of the specific entropy in Model B1 (see the description of the averaged procedure below). This distribution has the negative slope and therefore satisfies the Schwarzschild criterion for convection.

The nonconservative Model B2 is similar in many respects to the conservative Model B1. Model B2 also forms a turbulent quasi-steady flow pattern. Like in Model B1, the developed nonuniformities in the density frequently take the form of narrow filaments, which are extended in the radial direction. However, the amplitude and intensity of turbulent fluctuations in Model B2 are significantly reduced in comparison with Model B1. As the result, the rate of reconnection dissipation is smaller in Model B2 and the average magnetic field is stronger. The turbulent motions in Model B2 involve different MHD effects and are mainly supported by magnetic reconnections, magnetic buoyancy, and interchange instability. Convection motions are not developed in this model because of the absence of reconnection heat. The latter explains the less efficient turbulence observed in this model.

Our MHD models are time variable and, therefore, it is more practical to study the structure of these models by performing time and space averaging. In this way, we have constructed one-dimensional distributions of different quantities, averaging them over the

θ and ϕ directions. We have also averaged the obtained spatially averaged distributions over time, assuming the time-averaged interval $\tau \simeq 3t_{\text{ff}}$. Figure 3 shows the averaged radial profiles of selected quantities in Models B1 and B2 (solid and dotted lines, respectively). A comparison of these profiles shows certain differences in all quantities except in the accretion rates (see lower right panel in Fig. 3). These rates are close to each other and almost independent of the radius. The latter confirms that the considered flows are in quasi-steady states.

Model B2 shows a little steeper average profiles for ρ and P_g and a flatter profile of v in the inner and middle radial ranges, $R \lesssim 5R_{\text{in}}$, in comparison with Model B1. The profiles of P_m show almost the same slopes in both models, but the magnitude of P_m is by the factor of $\simeq 2$ larger in Model B2 than in Model B1. As discussed earlier, this difference in P_m can be explained by the less efficient dissipation of magnetic field in Model B2.

The presence and absence of the reconnection heat resulted in different temperatures in Models B1 and B2 (see left lower panel in Fig. 3). In agreement with a naive expectation, the conservative Model B1 has the larger temperature. At the same time, this model has a larger magnetic Mach number, $\mathcal{M}_m = v/\sqrt{c_s^2 + c_A^2}$, where $c_A = \sqrt{B^2/4\pi\rho}$ is the Alfvénic speed, and larger v in the inner region (see right top and right middle panels in Fig. 3). The latter two facts can not be simply understood using the analogy with Bondi-type flows in which lower \mathcal{M} and v correspond to hotter flows. It seems that the stronger magnetic field is responsible for the relative reduction of these quantities in Model B2.

The averaged radial structures of MHD Models B1 and B2 show noticeable differences from the radial structures of hydrodynamic Model A1 and self-similar solution (A9) (see Fig. 3). The MHD flows have the flattened density profiles. In terms of the power-law distribution $\rho \propto R^{-\sigma}$, Models B1 and B2 have $\sigma \approx 0.7$, whereas Model A1 and solution (A9) have respectively $\sigma \approx 1.3$ and $\sigma = 1.5$ (see left upper panel in Fig. 3). Similarly, Models B1 and B2 have the flattened profiles of $P_g \propto R^{-\eta}$ in which $\eta \approx 1.5$, whereas Model A1 and solution (A9) have $\eta \approx 2.2$ and $\eta = 2.5$, respectively (see left middle panel in Fig. 3). Other differences between hydrodynamic and MHD flows include the larger temperatures and reduced accretion velocities in the latter flows (see left lower and right middle panels in Fig. 3). The accretion rates in Models B1 and B2 show an $\simeq 10\%$ reduction with respect to Model A1 (see right lower panel in Fig. 3). This is a clear indication that turbulent MHD accretion flows have reduced accretion rates.

3.3. Supersonic MHD Flows

Supersonic MHD flows are represented by Models C1 and C2 (see Table 1). These models have been initiated from the supersonic hydrodynamic Model A4 by injecting a loop magnetic field at R_{inj} . Similar to the subsonic MHD models (see §3.2), Models C1 and C2 have approached quasi-steady states after passing through the transient phases. However, the transient phases in these models show some differences: the developed temporal shocks and waves are downshifted by the supersonic inflow and never reached the outer boundary R_{out} . In quasi-steady states, each of these models obtains a new feature—a quasi-steady shock. This shock divides the flows into two regions: the outer and inner, which have super-fast and sub-fast-magnetosonic accretion velocities, respectively. In the outer region, the flows are radial and laminar. The magnetic field is dominated by the radial component; this is quickly increased inward as $B \propto R^{-2}$. No significant field dissipation and reconnections have been observed in this region. In the inner region, on the other hand, reconnections become important and the flow is turbulent. The quasi-steady shocks in both Models C1 and C2 can be classified as Alfvénic shocks; they change the orientation of magnetic lines, but leave the field strength almost unchanged. Right after the completion of the transient phases, these shocks have been located at $R \simeq 2R_{\text{in}}$ in both Models C1 and C2.

During the subsequent evolution, Models C1 and C2 have been slowly evolved on the time scales $\gg t_{\text{ff}}$. As a result of this evolution, the inner regions in these models have been expanded, and, consequently, the Alfvénic shocks have slowly moved outward. The shock moves relatively faster in the case of the conservative Model C1 and slower in the case of the nonconservative Model C2. Specifically, during the evolution time $t \simeq 40t_{\text{ff}}$ counted from the end of the transient phases, the shock has propagated a distance of $\simeq 6R_{\text{in}}$ in Model C1 and the distance $\simeq R_{\text{in}}$ in Model C2. It is worth noting that these slowly moving Alfvénic shocks do not have analogy in hydrodynamic accretion flows. In the latter flows, any developed shocks are nonstationary and move either inward or outward, depending on the assumed conditions, on the timescale of $\sim t_{\text{ff}}$.²

Figure 10 illustrates the flow pattern in the conservative Model C1, showing the velocity streamlines projected onto the equatorial plane. The Alfvénic shock is located at $R \approx 7R_{\text{in}}$ in the shown moment. Two flow regions can be clearly distinguished: the pre-shock laminar outer and post-shock turbulent inner regions. Figure 11 shows magnetic lines that correspond to the flow pattern shown in Figure 10. In the pre-shock region, magnetic lines are purely radial, but oppositely directed in different sectors (see Fig. 2). These lines do not experience reconnections because of the purely radial flow pattern. In the post-shock region, magnetic

²We do not consider the radiative shocks here, which can be (quasi) steady.

lines are tangled because of the turbulent flow pattern and frequently reconnected.

The difference in Alfvénic shock motions in Models C1 and C2 suggests that there are two different mechanisms that cause these motions. Model C1, which includes the reconnection heat, develops a convection in the post-shock region, similar to the convection in Model B1. This convection transports the heat outward, causing the relatively fast expansion of the inner region and faster motion of the shock. This mechanism, however, is not suitable for Model C2, which does not include the reconnection heat and does not develop convection. Instead, the shock motion in Model C2 can be explained by magnetic buoyancy, which acts in the post-shock region in a manner similar to the action of magnetic buoyancy in Model B2. As a result, the magnetic field and energy are transported outward, forcing the inner region to expand and move the shock outward. The slower expansion of the post-shock in Model B2 is explained by the less-efficient energy transport provided by magnetic buoyancy.

The radial distributions of selected quantities in Models C1 and C2 are shown in Figure 4 by solid and dotted lines, respectively. These distributions have been obtained employing the averaging techniques described in §3.3 in which the time-averaged interval is chosen to be smaller, $\tau \simeq 0.1 t_{\text{ff}}$, to avoid “washing out” the moving shocks. One can clearly see that the structure of Models C1 and C2 changes quite sharply at the Alfvénic shocks, whose locations at the shown moments are $R \approx 7.5 R_{\text{in}}$ and $\approx 3 R_{\text{in}}$, respectively.

The outer regions in Models C1 and C2 are almost identical to each other and similar to the outer part of Model A4 (the dashed lines in Fig. 4). This can be seen in the distributions of all quantities except for the magnetic Mach number \mathcal{M}_{m} (see right upper panel in Fig. 4). Models C1 and C2 include strong magnetic fields that significantly reduce \mathcal{M}_{m} (but still $\mathcal{M}_{\text{m}} > 1$ before the shocks), whereas the accretion velocities remain almost the same as in hydrodynamic Model A4 (see right middle panel in Fig. 4). Note the interesting behavior of P_{g} and P_{m} in these models (see left middle panel in Fig. 4). The values of P_{g} before the shocks in the MHD models closely follow the corresponding value in Model A4. The values of P_{m} , which are started from the subequipartition level at R_{inj} , $\beta = 10$, quickly exceed the equipartition level, increasing inward as $P_{\text{m}} \propto R^{-4}$. In the case of Model C2, $\beta \approx 0.1$ just before the shock and the energy of the flow is dominated by the kinetic and magnetic energies, which are of approximately equal magnitudes.

The inner turbulent regions in Models C1 and C2 are sub-fast-magnetosonic, $\mathcal{M}_{\text{m}} < 1$, and have Alfvénic or moderately super-Alfvénic accretion velocities, $v \gtrsim c_a$. These regions are more dense, more hot, and have lower accretion velocities than the corresponding part of Model A4 (see Fig. 4). Magnetic reconnections are important here; they support turbulence and provide dissipation of the magnetic fields. This dissipation noticeably reduces the slope of P_{m} with respect to the corresponding slope in the outer region of the flow where the

dissipation is negligibly small. In the case of Model C2, the power-law index η for the magnetic pressure distribution $P_m \propto R^{-\eta}$ is changed from $\eta = 4$ in the outer part to $\eta \approx 3$ in the inner part of the flow (see left middle panel in Fig. 4).

4. Discussion and Conclusions

We have numerically investigated quasi-steady MHD spherical accretion flows with imposed small-scale magnetic fields. We have confirmed the previous theoretical expectation and numerical results such that the flows are turbulent and have radial structures different from the Bondi-type accretion flows (e.g., Shvartsman 1971; IN). Turbulence in the MHD flows is developed and supported by the interchange instability, thermal convection, and various magnetic interactions, including magnetic reconnections and buoyancy. The highly nonuniform release of energy in reconnections, which is, in fact, the release of the gravitational energy converted and stored in the form of magnetic field, makes these flows so special and different from the laminar and stable Bondi-type flows (however, see Kovalenko & Eremin 1998). We have found that magnetic buoyancy, in addition to thermal convection, can play an important role in the modification of the flow structure, especially in the case of nonconservative (or radiatively efficient) flows in which the convection could not be developed.

The most important consequence of turbulence in our MHD models, both conservative and nonconservative, is the modification of the radial flow structure. Figure 3 demonstrates this modification. Turbulent subsonic MHD Models B1 and B2 have the flattened time-averaged density profiles, higher temperatures, and lower accretion velocities in comparison with their hydrodynamic counterpart Model A1. These properties make Models B1 and B2 more like spherical CDAFs (see IN) than Bondi accretion flows. The theory of spherical CDAFs predicts the flattened power-law density profile $\rho \propto R^{-\sigma}$ in which $\sigma = 0.5$. Models B1 and B2 have profiles close to this, but more steep, $\sigma \approx 0.7$. These steeper profiles can be explained by the influence of the inner boundary condition in our numerical models, whereas the analytic CDAF solution is “boundary free.” Abramowicz *et al.* (2002) argued that the proximity of the black hole absorbing boundary makes the inner regions of CDAFs to be advection dominated. In particular, they demonstrated that viscous rotating CDAFs become advection dominated inside ~ 50 to 100 gravitational radii. Our numerical models have a rather small radial range, $R_{\text{out}}/R_{\text{in}} = 10$, and, therefore, the effects of the inner boundary can be significant.

Turbulent Models B1 and B2 have shown the reduction of the accretion rates in comparison with laminar Model A1 (see right lower panel in Fig. 3). This result qualitatively

confirms the predicted reduction of the accretion rate in spherical CDAFs (see eq. [1]). However, the actual reduction of the accretion rates, which is about 10%, shows a poor quantitative agreement with estimate (1). We explain this poor agreement by the limited radial range in our models, whereas estimate (1) was obtained in the limit $R_{\text{out}} \gg R_{\text{in}}$.

The conservative and nonconservative subsonic MHD models (Models B1 and B2, respectively) are turbulent, however, the turbulence properties in these models are different. In the conservative model, the turbulent motions are more intensive and mainly supported by thermal convection, which makes this model similar to spherical CDAFs. The nonconservative model has less intensive turbulence, which is supported through various magnetic interactions in which magnetic buoyancy seems to be dominated. In some respect, the magnetic buoyancy acts similar to the thermal convection; it also transports (magnetic) energy outward. This transport can explain the flattened density profile in the nonconservative model, like the convection in spherical CDAFs (see IN). However, the energy transport provided by magnetic buoyancy is less efficient and much weaker than the convection transport.

Our supersonic MHD accretion flows (Models C1 and C2) have been initiated by injecting a low entropy matter into the computational domain. These flows form quasi-steady Alfvénic shocks that separate the laminar super-fast-magnetosonic outer inflows and the post-shock turbulent nearly Alfvénic inner inflows. We have found that the averaged flow pattern in these models is not steady on the large time scale $\gg t_{\text{ff}}$. The post-shock regions gradually expand, forcing the Alfvénic shocks to move outward. These regions are quite similar to the subsonic MHD flows in Models B1 and B2, and, therefore, the gradual expansion of these regions can be explained by the outward energy flux provided by convection and/or magnetic buoyancy. We have found that the Alfvénic shock moves significantly faster in the case of Model C1, which develops a convection in the post-shock region. The latter is consistent with our observation that the more intensive turbulence and, respectively, the larger outward energy flux happens in convective Model B1, rather than in nonconvective Model B2.

Based on our study of the supersonic MHD models, we conclude that *stationary* supersonic (or super-fast-magnetosonic) accretion flows cannot be realized in the presence of small-scale magnetic fields. This conclusion is equally applied to radiatively efficient and inefficient flows. Such supersonic flows will unavoidably create shocks at the equipartition radius and these shocks will be moved outward because of the action of convection and magnetic buoyancy, which are developed in turbulent post-shock regions of these flows. These post-shock regions will continue to expand and, on the large time scale, fill the entire accretion domain, causing the flows to be subsonic everywhere.

The wedge computational domain of our models has the limited opening angle (see

Fig. 1), and we use the specific boundary conditions in the angular directions (see Section 2.1) to minimize the influence of this limited-size domain. Definitely, the used boundary conditions could have some effects on the properties of the simulated MHD turbulence, for example, limiting the spatial scales and effecting the motions in the vicinity of the polar sliding boundaries. Other consequence of the employing this domain is the inability to simulate large scale magnetic structures, which can be developed during the reverse cascade of energy from small to large spatial scales in a MHD turbulence. This issue of the limited computational domain should be addressed in future works.

The accretion of mass in our MHD models is accompanied by the reconnection dissipation of the magnetic field in turbulent flows. The rate of dissipation is consistently regulated through feedback mechanisms that also regulate the intensity of the turbulence. To illustrate the dissipation process quantitatively, we consider the nonconservative MHD models in which the change of the time-averaged radial flux of the total energy

$$F_R = \int_{\Omega_0} R^2 q_R d\Omega \quad (13)$$

directly corresponds to the amount of dissipated magnetic energy. The integral in equation (13) is taken over the solid angle of the computational domain Ω_0 and the radial flux per unit square (see eq. [3]) is

$$q_R = \rho v_R \left(\frac{v^2}{2} + \epsilon + \frac{P}{\rho} + \frac{B^2}{4\pi\rho} - \frac{GM}{R} \right) - \frac{B_R}{4\pi} (\mathbf{v} \cdot \mathbf{B}). \quad (14)$$

The solid lines in Figure 12 represent the radial dependence of the total energy fluxes obtained in Models B2 and C2. These fluxes have been normalized to the flux $GM\dot{M}_{\text{in}}/R_{\text{in}}$. The dashed lines in Figure 10 correspond to the flux conservation $F_R = \text{const}$. The difference between the dashed and solid lines at a given R represents the amount of the energy dissipated in the radial range from R_{out} to R . Note that the energy dissipates in the whole volume in Model B2, whereas it dissipates only in the post-shock region and no energy dissipates in the pre-shock region in Model C2. The total amount of reconnection losses given in units of gravitational energy at R_{in} is about 6.5% in Model B2 and about 5% in Model C2.

The author gratefully thanks Ramesh Narayan and Igor Novikov for discussions, and Vasilij Beskin for usefull comments. This work was supported by the U.S. Department of Energy (DOE) Office of Inertial Confinement Fusion under Cooperative Agreement No. DE-FC52-92SF19460, the University of Rochester, the New York State Energy Research and Development Authority.

A. Some Analytic Solutions of Spherical Hydrodynamic Accretion Flows

In this paper, we have compared our numerical models and analytic solutions of spherical hydrodynamic accretion flows. We reproduce some relevant formulas for these solutions below.

Spherical, stationary, and isentropic hydrodynamic accretion flows are described by the continuity equation

$$\dot{M} = 4\pi R^2 \rho v, \quad (\text{A1})$$

Bernoulli's equation

$$\frac{v^2}{2} + \frac{\gamma}{\gamma - 1} \frac{P}{\rho} - \frac{GM}{R} = \text{constant}, \quad (\text{A2})$$

and the polytropic equation of state

$$P = K \rho^\gamma, \quad (\text{A3})$$

where P is the gas pressure, K is the polytropic constant, γ is the polytropic index, and \dot{M} is the accretion rate. Bondi (1952) solved these equations assuming that the flow is at rest and of the uniform density ρ_∞ , pressure P_∞ , and sound speed $c_\infty = \sqrt{\gamma P_\infty / \rho_\infty}$ at infinity. The Bondi solution depends on the spatial scale $R_B = 2GM/c_\infty^2$, called the Bondi or accretion radius, and can be expressed in the following implicit form that gives the radial dependence of ρ :

$$\lambda^2 \left(\frac{R_B}{R} \right)^4 \left(\frac{\rho_\infty}{\rho} \right)^2 + \frac{2}{\gamma - 1} \left[\left(\frac{\rho}{\rho_\infty} \right)^{\gamma-1} - 1 \right] - \frac{R_B}{R} = 0, \quad (\text{A4})$$

where $\lambda = \dot{M} / (4\pi R_B^2 \rho_\infty c_\infty)$ is the dimensionless accretion rate defined by the expression

$$\lambda = \left(\frac{1}{2} \right)^{\frac{5\gamma-3}{2(\gamma-1)}} \left(\frac{5-3\gamma}{4} \right)^{\frac{3\gamma-5}{2(\gamma-1)}}. \quad (\text{A5})$$

In the small-radii limit, $R \ll R_B$, the Bondi solution (A4) is represented by the asymptotic power-law distributions

$$\begin{aligned} v &\propto R^{-1/2}, \\ \rho &\propto R^{-3/2}, \\ P &\propto R^{-5/2}. \end{aligned} \quad (\text{A6})$$

In the case of $1 \leq \gamma < 5/3$, the Bondi solution (A4) describes transonic flows in which the Mach number

$$\mathcal{M} = \lambda \left(\frac{R_B}{R} \right)^2 \left(\frac{\rho_\infty}{\rho} \right)^{(\gamma+1)/2} \quad (\text{A7})$$

is zero at infinity and monotonically increases inward, approaching the infinite value at $R = 0$.

In the subsequent discussion, we shall consider only the case $\gamma = 5/3$, which is known to be the special case of the Bondi solution (A4). In this case, the flow is subsonic everywhere and $\mathcal{M} = 1$ only in the limit of $R \rightarrow 0$. However, such a “boundary free” solution is not practical for numerical applications and we have modified the Bondi solution to include the finite inner boundary radius $R_{\text{in}} > 0$ in which we require $\mathcal{M} = 1$. The modified Bondi solution is described by same equation (A4) and the same equation (A7) represents the Mach number, but a new λ is defined as follows:

$$\lambda = \left(\frac{1 + 3\delta}{4} \right)^2, \quad (\text{A8})$$

where $\delta = R_{\text{in}}/R_B$ is a free parameter; $0 < \delta < 1$. This modified solution approximates well our subsonic Model A1, assuming $\delta = 0.00371$ (short-dashed lines in Fig. 3).

In the case of $\gamma = 5/3$, equations (A1)-(A3) allow a self-similar solution, which requires the special outer boundary condition $c_\infty = 0$ or, equivalently, to set the constant on the right hand side of equation (A2) to zero. This solution reads

$$\begin{aligned} v &= \alpha \sqrt{GM/R}, \\ \rho &= \dot{M}/(4\pi\alpha\sqrt{GMR}^{3/2}), \\ P &= \frac{2}{5} \left(1 - \frac{\alpha^2}{2} \right) \frac{GM\rho}{R}, \end{aligned} \quad (\text{A9})$$

where α is a free parameter; $0 < \alpha < \sqrt{2}$. Solution (A9) can be subsonic or supersonic depending on α . This solution is characterized by the constant Mach number

$$\mathcal{M} = \alpha \sqrt{1.5/(1 - \alpha^2/2)}, \quad (\text{A10})$$

and it is supersonic at $1/\sqrt{2} < \alpha < \sqrt{2}$.

Another kind of supersonic solution in the special case of $\gamma = 5/3$ can be constructed assuming the outer boundary at some finite radius R_{out} in which we require $\mathcal{M} = 1$. This solution takes the form

$$\tilde{\lambda}^2 \left(\frac{\tilde{R}_B}{R} \right)^4 \left(\frac{\rho_{\text{out}}}{\rho} \right)^2 + 3 \left[\left(\frac{\rho}{\rho_{\text{out}}} \right)^{2/3} - 1 \right] - \frac{\tilde{R}_B}{R} + \frac{1}{\tilde{\delta}} - 1 = 0, \quad (\text{A11})$$

where $\tilde{R}_B = 2GM/c_{\text{out}}^2$ and $\tilde{\delta} = R_{\text{out}}/\tilde{R}_B$, and we denote ρ_{out} and c_{out} to be the density and sound speed at R_{out} , respectively. Solution (A11) exists for $0 < \tilde{\delta} \leq 1/4$. The dimensionless

accretion rate $\tilde{\lambda} = \dot{M}/(4\pi\tilde{R}_B^2\rho_{\text{out}}c_{\text{out}})$ can be expressed in the form

$$\tilde{\lambda} = \tilde{\delta}^2. \quad (\text{A12})$$

The Mach number in solution (A11)

$$\mathcal{M} = \tilde{\lambda} \left(\frac{\tilde{R}_B}{R} \right)^2 \left(\frac{\rho_{\text{out}}}{\rho} \right)^{4/3} \quad (\text{A13})$$

monotonically increases inward and approaches the asymptotic value \mathcal{M}_0 at $R \ll R_{\text{out}}$. In the limit $\tilde{\delta} \ll 1$, one gets $\mathcal{M}_0 = \tilde{\delta}^{-2/3}$. In the case of marginal $\tilde{\delta} = 1/4$, one gets $\mathcal{M} = \mathcal{M}_0 = 1$ and solution (A11) becomes equivalent to the self-similar solution (A9) in which $\alpha = 1/\sqrt{2}$. Solution (A11) approximates well our supersonic Model A4, assuming $\tilde{\delta} = 0.071$ (short-dashed lines in Fig. 4).

REFERENCES

- Abramowicz, M. A., Igumenshchev, I. V., Quataert, E., & Narayan, R. 2002, *ApJ*, 565, 1101
- Agol, E., & Kamionkowski, M. 2002, *MNRAS*, 334, 553
- Baganoff, F. K., et al. 2001, *Nature*, 413, 45
- Baganoff, F. K., et al. 2003, *ApJ*, 591, 891
- Belloni, T., Zampieri, L. & Campana, S. 1997, *A&A*, 319, 525
- Bisnovatyi-Kogan, G. S., & Ruzmaikin, A. A. 1974, *Ap&SS*, 28, 45
- Bisnovatyi-Kogan, G. S., & Lovelace, R. V. E. 1997, *ApJ*, 486, L43
- Bisnovatyi-Kogan, G. S., & Lovelace, R. V. E. 2000, *ApJ*, 529, 978
- Blaes, O., & Madau, P. 1993, *ApJ*, 403, 690
- Bondi, H. 1952, *MNRAS*, 112, 195
- Cabral, B., & Leedom, L. 1993, *Computer Graphics: Proceedings: Annual Conference Series 1993: SIGGRAPH 93* (New York: Association for Computing Machinery), 263
- Esin, A. A., Narayan, R., Ostriker, E., & Yi, I. 1996, *ApJ*, 465, 312
- Frank, J., King, A., & Raine, D. 1992, *Accretion Power in Astrophysics* (Cambridge Univ. Press, Cambridge)
- Fujita, Y., Inoue, S., Nakamura, T., Manmoto, T., & Nakamura, K. E. 1998, *ApJ*, 495, L85
- Ghez, A. M., et al. 2003, *ApJ*, 586L, 127
- Ho, L. C., Terashima, Y., & Okajima T. 2003, *ApJ*, 587L, 35
- Igumenshchev, I. V., & Abramowicz, M. A. 1999, *MNRAS*, 303, 309
- Igumenshchev, I. V., & Narayan, R. 2002, *ApJ*, 566, 137 (IN)
- Igumenshchev, I. V., Narayan, R., & Abramowicz, M. A. 2003, *ApJ*, 592, 1042
- Illarionov, A. F., & Sunyaev R. A. 1975, *A&A*, 39, 185
- Kato, S., Fukue, J., & Mineshige, S. 1998, *Black-Hole Accretion Disks* (Kyoto: Kyoto Univ. Press)

- Katz J. I., 1977, ApJ, 215, 265
- Kovalenko, I. G., & Eremin, M. A. 1998, MNRAS, 298, 861
- Krumholz, M. R., McKee, C. F., & Klein, C. F. 2005, ApJ, 618, 757
- Landau, L. D., & Lifshitz, E. M. 1987, *Electrodynamics of Continuous Media*. Pergamon Press, Oxford
- Marković, D. 1995, MNRAS, 277, 11
- Melia, F. 1992, ApJ, 387, L25
- Pen, U.-L., Matzner, C. D., & Wong, S. 2003, ApJ, 596, L207
- Perna, R., Narayan, R., Rybicki, G., Stella, L., & Treves, A. 2003, ApJ, 594, 936
- Narayan, R., Igumenshchev, I. V., & Abramowicz, M. A. 2000, ApJ, 539, 798
- Quataert, E. 2002, ApJ, 575, 855
- Quataert, E., & Gruzinov, A. 1999, ApJ, 520, 248
- Quataert, E., & Gruzinov, A. 2000, ApJ, 539, 809
- Shadmehri, M. 2004, A&A, 424, 379
- Shakura, N. I. 1972, AZh, 49, 921
- Shapiro, S. L., & Salpeter, E. E. 1975, ApJ, 198, 671
- Shvartsman, V. F. 1971, Soviet Astron. J., 15, 37
- Soria, R., Fabiano, G., Graham, A. W., Baldi, A., Elvis, M., Jerjen, H., Pellegrini, S., & Siemiginowska, A. 2006, ApJ, 40, 126
- Thorne, K. S., Price, R. H., & MacDonald, D. H. 1986, *Black Holes: The Membrane Paradigm*
- Toropin, Yu. M., Toropina, O. D., Savelyev, V. V., Romanova, M. M., Chechetkin, V. M., & Lovelace, R. V. E. 1999, ApJ, 517, 906
- Toropina, O. D., Romanova, M. M., Toropin, Yu. M., & Lovelace, R. V. E. 2003, ApJ, 953, 472
- Treves, A., & Colpi, M. 1991, A&A, 241, 107

Turolla, R., Zampieri, L., Colpi, M., & Treves, A. 1994, ApJ, 426, L35

Table 1. Parameters of the Models

| Model | ϵ_0^{a} | β_0^{b} | Reconnection heat | Field topology |
|-------|-------------------------|----------------------|-------------------|----------------|
| A1 | 1.2 | 0 | — | — |
| A2 | 1.2 | 10^2 | — | Toroidal |
| A3 | 1.2 | 30 | — | Radial |
| A4 | 0.3 | 0 | — | — |
| B1 | 1.2 | 10 | Included | Loop |
| B2 | 1.2 | 10 | Not included | Loop |
| C1 | 0.3 | 10 | Included | Loop |
| C2 | 0.3 | 10 | Not included | Loop |

^aCharacterizes the specific internal energy of the injected mass given in units of ϵ_{vir} (see eq. [5]). The flows with $\epsilon_0 = 1.2$ are subsonic and $\epsilon_0 = 0.3$ are supersonic.

^bCharacterizes the initial or injected magnetic field strength and is defined in eq. (11).

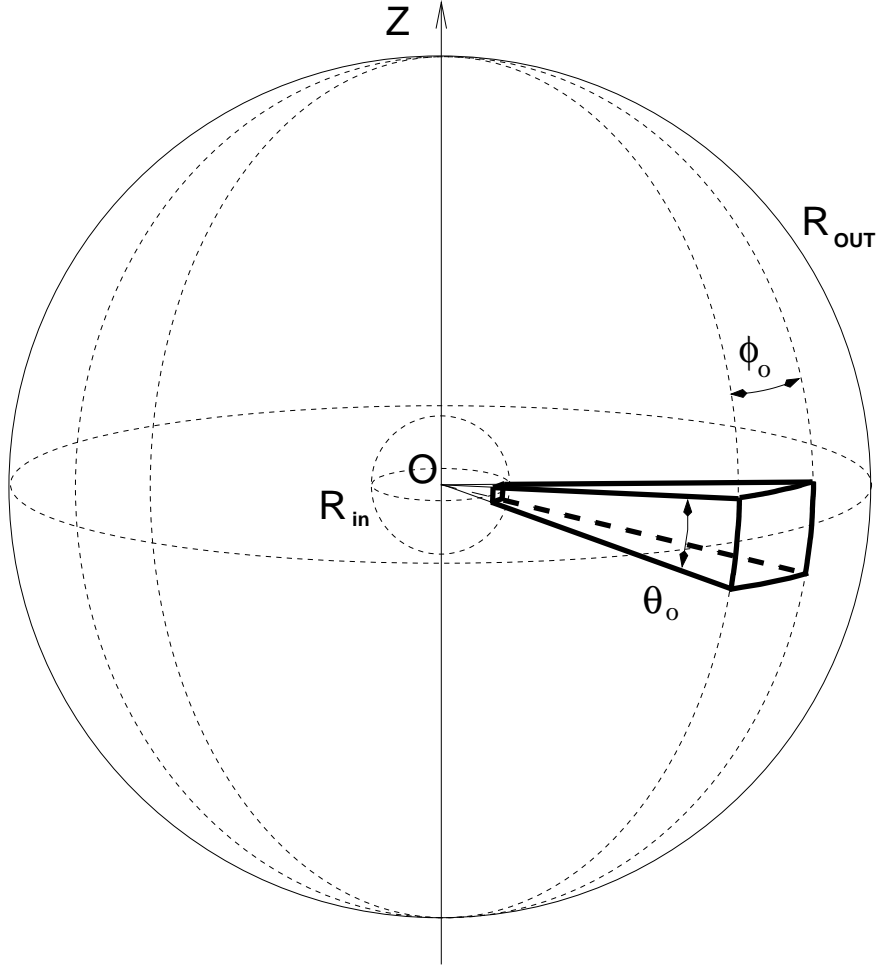


Fig. 1.— Geometry of the computational domain used in the simulations. The domain is extended from R_{in} to R_{out} in the radial direction ($R_{\text{out}}/R_{\text{in}} = 10$) and spans the angles θ_0 and ϕ_0 in the polar and azimuthal directions, respectively ($\theta_0 = \phi_0 = \pi/16$). The source of gravity is located in the origin.

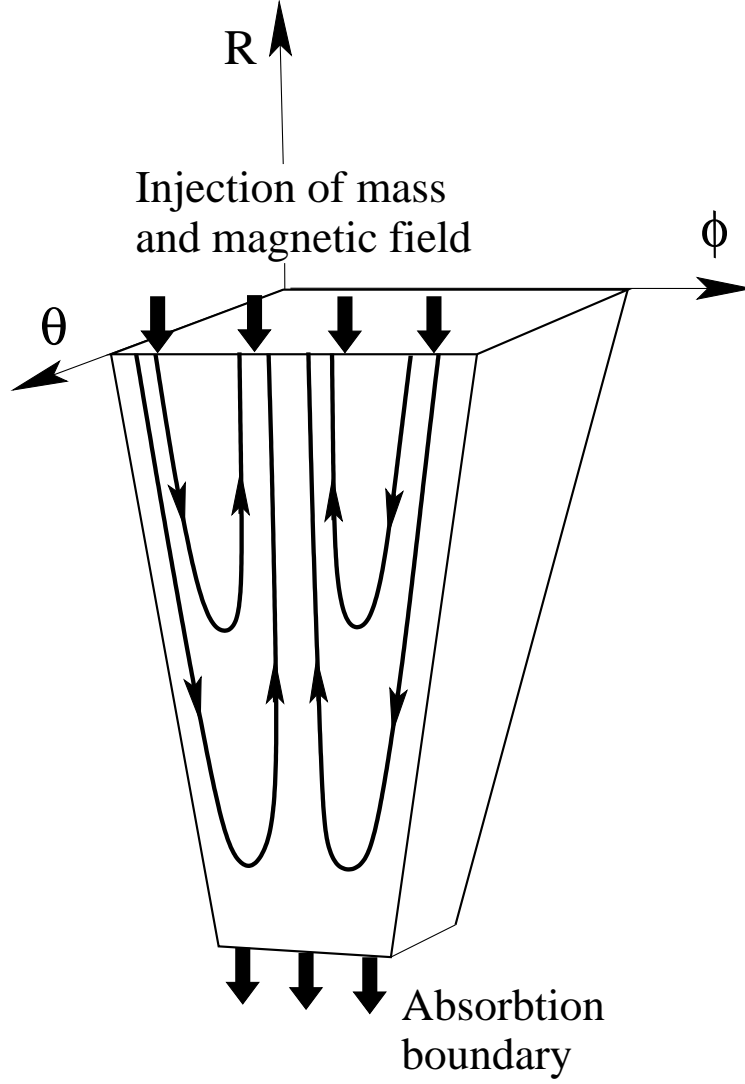


Fig. 2.— Schematic illustration of the simulation design. A three-dimensional MHD accretion flow is formed as the result of a steady injection of mass and magnetic field in the vicinity of the outer radial boundary in the wedge computational domain. The geometry of the injected field is represented by magnetic lines (thick solid lines with arrows). The accretion flow with a frozen-in magnetic field is absorbed at the inner radial boundary.

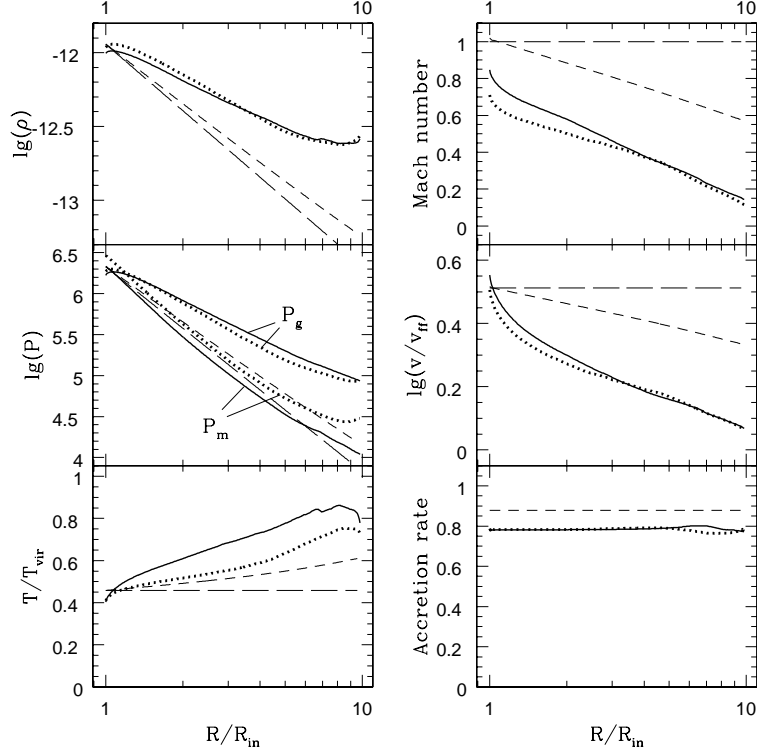


Fig. 3.— Radial structure of the subsonic accretion flows in Models A1 (short-dashed lines), B1 (solid lines), B2 (dotted lines), and self-similar solution (long-dashed lines, see eq. [A9]). Hydrodynamic Model A1 is steady; turbulent MHD Models B1 and B2 are shown in quasi-steady states. All plotted quantities in the turbulent models—the density ρ , gas and magnetic pressures P_g and P_m , temperature T , magnetic Mach number \mathcal{M}_m , accretion velocity v , and mass accretion rate \dot{M} —have been averaged over the angles θ and ϕ and over the time interval $\tau \simeq 3t_{\text{ff}}$.

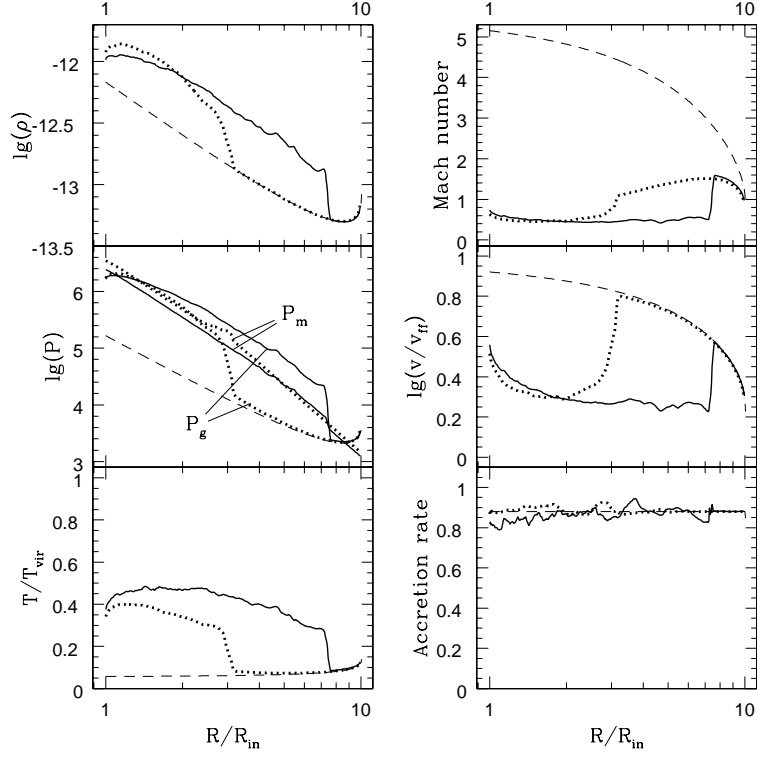


Fig. 4.— Radial structure of the supersonic accretion flows in Models A4 (short-dashed lines), C1 (solid lines), and C2 (dotted lines). Hydrodynamic Model A4 is steady; turbulent MHD Models C1 and C2 are shown in quasi-steady states. All plotted quantities in the turbulent models—the density ρ , gas and magnetic pressures P_g and P_m , temperature T , magnetic Mach number \mathcal{M}_m , accretion velocity v , and mass accretion rate \dot{M} —have been averaged over the angles θ and ϕ and over the time interval $\tau \simeq 0.1 t_{\text{ff}}$. The MHD models have slowly moving outward Alfvénic shocks, which are located at the shown moment at $R \approx 7.5 R_{\text{in}}$ in Model C1 and $R \approx 3 R_{\text{in}}$ in Model C2.

Fig. 5.— Snapshot of the density distribution in Model B1 in the equatorial plane. The source of gravity is located on the left, outside of the shown cross-section of the computational domain (for a general view see Fig. 1). The shown radial range $R_{\text{out}}/R_{\text{in}} = 10$ represents the fully simulated domain. The mass and magnetic field are steadily injected near the outer radial boundary on the right. The color bar on the left indicates the scale for $\log \rho$ (in arbitrary units). The model is turbulent and shown in a quasi-steady state. The fluctuations in the density are caused mainly by nonuniform reconnection heat and supported by convection motions.

Fig. 6.— Snapshot of velocity streamlines in Model B1 in the equatorial plane in the same moment as in Fig. 5. The component of the streamlines parallel to the plane is shown. The flow pattern consists of the radially (horizontal in this view) extended narrow inflowing/outflowing streams and small-scale vortices. The streamlines have been plotted using the line integral convolution method of Cabral & Leedom (1993).

Fig. 7.— Snapshot of magnetic lines in Model B1 in the equatorial plane in the same moment as in Fig. 5. The component of the field lines parallel to the plane is shown. One can see many magnetic loops stretched in the radial (horizontal in this view) direction. These loops are the result of convection and interchange instability.

Fig. 8.— Snapshot of the distribution of the plasma $\beta \equiv P_g/P_m$ in Model B1 in the equatorial plane in the same moment as in Fig. 5. The color bar on the left indicates the scale for $\log \beta$. Small-scale regions of large β , or weak magnetic fields, correspond to regions of reconnection and dissipation of magnetic energy. The large number of these regions indicates the high efficiency of the reconnection dissipation. Regions of low β , or strong magnetic fields, are typically elongated in the radial (horizontal in this view) direction and associated with the inflowing streams.

Fig. 9.— Snapshot of the distribution of specific entropy s in Model B1 in the equatorial plane in the same moment as in Fig. 5. The color bar on the left indicates the scale for $\log s$ (in arbitrary units). Regions of large s represent hot convective bubbles and streams, which have positive buoyancy and typically move outward. Regions of low s correspond to relatively cold inflowing matter. On average, the specific entropy is increased inward.

Fig. 10.— Snapshot of velocity streamlines in supersonic Model C1 in the equatorial plane. The component of the streamlines parallel to the plane is shown. The flow pattern consists of two regions: the laminar super-fast-magnetosonic pre-shock (outer, on the right in this view) region and turbulent/convective post-shock (inner, on the left in this view) region. A quasi-steady Alfvénic shock separates these two regions and is located at $R \approx 7 R_{\text{in}}$ in the shown moment. This shock slowly moves outward.

Fig. 11.— Snapshot of magnetic lines in supersonic Model C1 in the equatorial plane in the same moment as in Fig. 10. The component of the field lines parallel to the plane is shown. The field lines are purely radial (but oppositely directed in different sectors, see Fig. 2) and do not experience reconnections in the laminar pre-shock region (see capture to Fig. 10). The tangled field lines in the post-shock region are the result of convection and interchange instability.

Fig. 12.— Radial distribution of the time-averaged total energy flux F_R normalized to the flux $GM\dot{M}_{\text{in}}/R_{\text{in}}$ in Models B2 and C2 (solid lines). Reduction of F_R with respect to its value at the outer boundary (shown by dashed lines) represent losses of magnetic energy in reconnections. Supersonic Model C2 is shown at the moment, which corresponds to the Alfvénic shock position $R \approx 4.7 R_{\text{in}}$. Note the absence of energy losses in the laminar pre-shock region in Model C2.

This figure "f5.jpg" is available in "jpg" format from:

<http://arxiv.org/ps/astro-ph/0606195v1>

This figure "f6.jpg" is available in "jpg" format from:

<http://arxiv.org/ps/astro-ph/0606195v1>

This figure "f7.jpg" is available in "jpg" format from:

<http://arxiv.org/ps/astro-ph/0606195v1>

This figure "f8.jpg" is available in "jpg" format from:

<http://arxiv.org/ps/astro-ph/0606195v1>

This figure "f9.jpg" is available in "jpg" format from:

<http://arxiv.org/ps/astro-ph/0606195v1>

This figure "f10.jpg" is available in "jpg" format from:

<http://arxiv.org/ps/astro-ph/0606195v1>

This figure "f11.jpg" is available in "jpg" format from:

<http://arxiv.org/ps/astro-ph/0606195v1>

This figure "f12.jpg" is available in "jpg" format from:

<http://arxiv.org/ps/astro-ph/0606195v1>